JACS Au
AN OPEN ACCESS JOURNAL OF THE AMERICAN CHEMICAL SOCIETY



pubs.acs.org/jacsau
Article

# PET Imaging of Innate Immune Activation Using $^{11}$C Radiotracers Targeting GPR84

Mausam Kalita, Jun Hyung Park, Renesmee Chenting Kuo, Samira Hayee, Sara Marsango, Valentina Straniero, Israt S. Alam, Angelie Rivera-Rodriguez, Mallesh Pandrala, Mackenzie L. Carlson, Samantha T. Reyes, Isaac M. Jackson, Lorenzo Suigo, Audrey Luo, Sydney C. Nagy, Ermanno Valoti, Graeme Milligan, Frezghi Habte, Bin Shen, and Michelle L. James*

Cite This: JACS Au 2023, 3, 3297−3310

Read Online

ACCESS | Metrics & More | Article Recommendations | Supporting Information

**ABSTRACT:** Chronic innate immune activation is a key hallmark of many neurological diseases and is known to result in the upregulation of GPR84 in myeloid cells (macrophages, microglia, and monocytes). As such, GPR84 can potentially serve as a sensor of proinflammatory innate immune responses. To assess the utility of GPR84 as an imaging biomarker, we synthesized **$^{11}$C-MGX-10S** and **$^{11}$C-MGX-11S** *via* carbon-11 alkylation for use as positron emission tomography (PET) tracers targeting this receptor. *In vitro* experiments demonstrated significantly higher binding of both radiotracers to hGPR84-HEK293 cells than that of parental control HEK293 cells. Co-incubation with the GPR84 antagonist GLPG1205 reduced the binding of both radiotracers by >90%, demonstrating their high specificity for GPR84 *in vitro*. *In vivo* assessment of each radiotracer *via* PET imaging of healthy mice illustrated the superior brain uptake and pharmacokinetics of **$^{11}$C-MGX-10S** compared to **$^{11}$C-MGX-11S**. Subsequent use of **$^{11}$C-MGX-10S** to image a well-established mouse model of systemic and neuro-inflammation revealed a high PET signal in affected tissues, including the brain, liver, lung, and spleen. *In vivo* specificity of **$^{11}$C-MGX-10S** for GPR84 was confirmed by the administration of GLPG1205 followed by radiotracer injection. When compared with $^{11}$C-DPA-713—an existing radiotracer used to image innate immune activation in clinical research studies—**$^{11}$C-MGX-10S** has multiple advantages, including its higher binding signal in inflamed tissues in the CNS and periphery and low background signal in healthy saline-treated subjects. The pronounced uptake of **$^{11}$C-MGX-10S** during inflammation, its high specificity for GPR84, and suitable pharmacokinetics strongly support further investigation of **$^{11}$C-MGX-10S** for imaging GPR84-positive myeloid cells associated with innate immune activation in animal models of inflammatory diseases and human neuropathology.

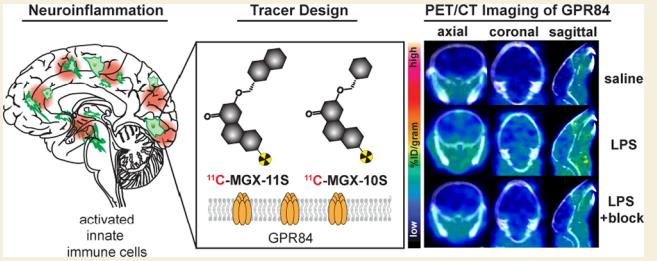


**KEYWORDS:** *$^{11}$C-radiotracers, positron emission tomography, imaging, innate immune activation, neuroinflammation, GPR84 biomarker*

## INTRODUCTION

Neuroinflammation is one of the cardinal features of multiple central nervous system (CNS) diseases, including Alzheimer's disease (AD), multiple sclerosis (MS), and stroke.[1−4] Brain-innate immune dysfunction upregulates a plethora of receptors or biomarkers that can serve as a barometer of neuro-inflammation.[5,6] Positron emission tomography (PET)—a highly sensitive molecular imaging modality—is well suited to measure these biomarkers, expressed on innate immune cells at low concentrations.[7] Accurate quantification of neuroinflammation *via* PET requires reliable biomarkers. Many of the currently available and emerging PET imaging biomarkers of neuroinflammation are limited by their unknown functional roles in diseases of interest, genetic polymorphisms that weaken the binding of some PET tracers to these targets, and/or their suboptimal specificity for deleterious innate immune responses. For example, translocator protein 18 kDa (TSPO)—the most widely studied biomarker for microglial/myeloid cell activation—is expressed in a broad spectrum of immune cells, astrocytes, cancer cells, and endothelial cells.[8] This lack of cellular-specificity, seen also with other emerging PET biomarkers of interest (CB2, P2X7, and MMP), complicates image analysis and the interpretation of such images. Moreover, polymorphisms in the *tspo* gene can confound the quantification of neuroinflammation due to interindividual variability in the binding affinities for certain TSPO PET tracers.[9] There is thus a critical need to generate

Received: August 3, 2023
Revised: November 2, 2023
Accepted: November 6, 2023
Published: December 1, 2023

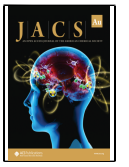





https://doi.org/10.1021/jacsau.3c00435
JACS Au 2023, 3, 3297−3310

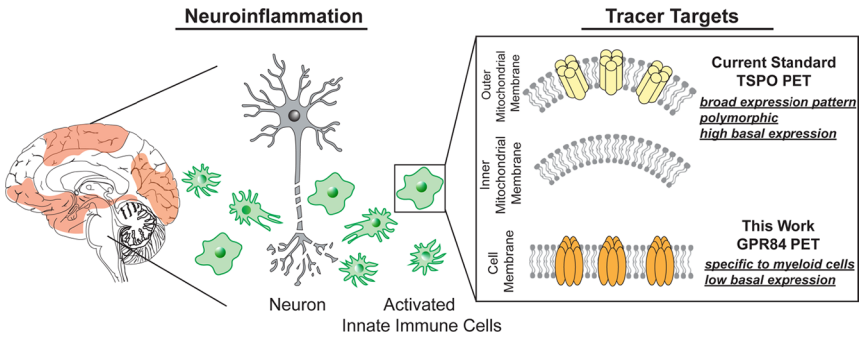


**Figure 1.** Neuroinflammation PET. Many widely used neuroinflammation PET radiotracers target the translocator protein 18 kDa (TSPO)—a nonspecific, polymorphic biomarker with relatively high basal expression. We sought to mitigate these issues by developing radiotracers for GPR84, a myeloid cell specific biomarker with low basal expression.

**Scheme 1. Chemical Synthesis of the Precursors and Cold Standards**

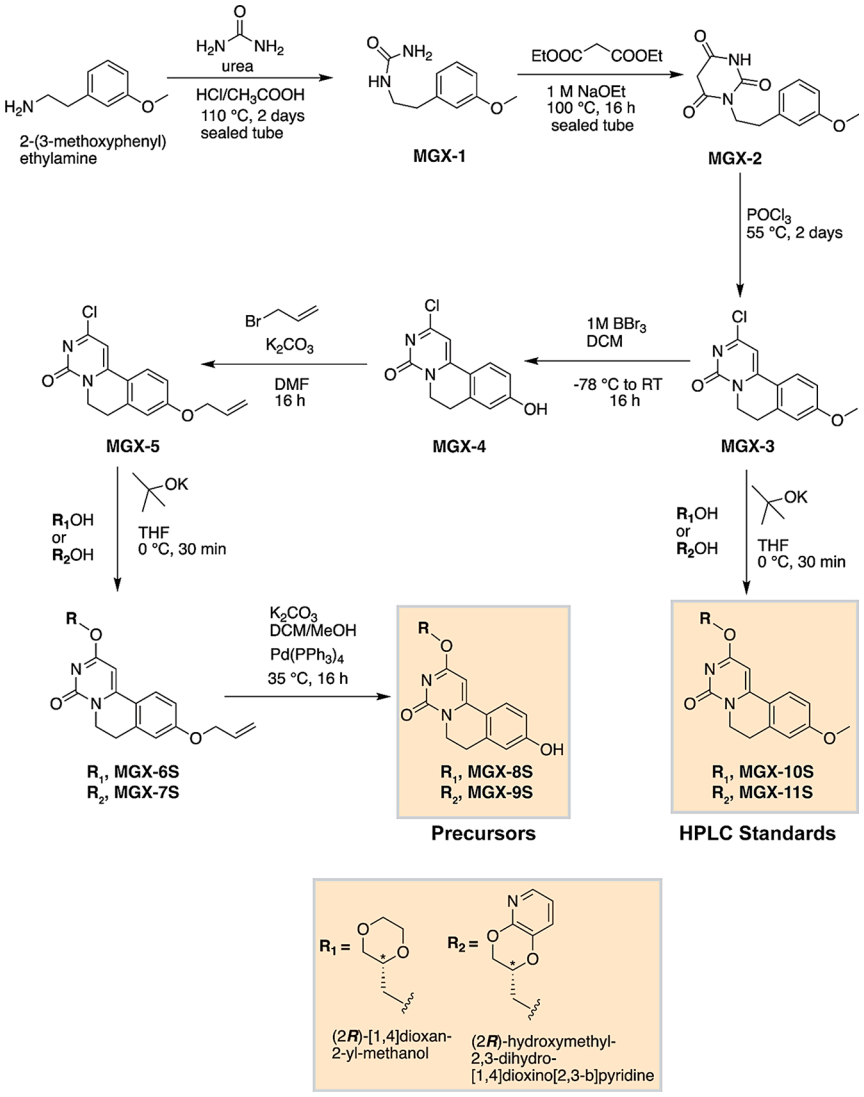


PET tracers for biomarkers that do not have genetic polymorphisms affecting binding and that are exclusively expressed in activated myeloid cells. Such radiotracers could enable more accurate quantification and staging of innate immune activation *in vivo* in many different diseases longitudinally, in addition to noninvasive assessment of response to novel immunomodulatory therapies.

GPR84, a seven-transmembrane domain orphan G-protein coupled receptor, is a new promising biomarker of innate immune activation.[10,11] The predominant expression of GPR84 on microglia in the CNS and peripheral myeloid cells (macrophages, monocytes, and neutrophils) make it an excellent candidate biomarker of innate immune responses.[12,13] Importantly, CNS injury and inflammatory


https://doi.org/10.1021/jacsau.3c00435
JACS Au 2023, 3, 3297−3310

stimuli are known to induce significant upregulation of GPR84 expression on pro-inflammatory microglia. For example, mice suffering from endotoxemia exhibit elevated GPR84 on microglia and, to a lesser extent, subpopulations of peripheral macrophages and monocytes.[14] Microglial GPR84 upregulation was also reported in the APP/PS1 transgenic AD mouse model, where GPR84 senses an elusive ligand that recruits microglia to amyloid plaques.[15] Similarly elevated microglial *gpr84* mRNA has been reported in the brain and white matter of the spinal cord in experimental autoimmune encephalomyelitis (EAE) mice, a model of multiple sclerosis. Specifically, the number of *gpr84* expressing activated microglia in the spinal cord tends to increase with EAE disease severity.[12] Additionally, in a mouse model of partial sciatic nerve ligation, *gpr84* mRNA expression in peripheral macrophages was upregulated in the sciatic nerve and spinal cord on days 7 and 21 while *gpr84* knockout mice displayed reduced neuropathic pain.[16] The restricted expression of GPR84 to myeloid cells[13] affords advantages to imaging this biomarker over others, such as TSPO, which have broader expression profiles (Figure 1).[17] The combination of increased GPR84 expression upon myeloid cell activation, its cellular specificity, and low basal expression motivated us to develop GPR84 radiotracers. Importantly, although the immunoregulatory characteristics of GPR84 make it a viable PET biomarker for imaging both general inflammation and neuroinflammation, there are currently no CNS-penetrable GPR84 PET tracers available.

While GPR84 is an orphan receptor without a known endogenous ligand, synthetic [1,4]*d*ioxan-2-ylmethoxy)-6,7-*d*i*h*ydro*p*yrimido[6,1-*a*]*i*soquinolin-4-one (DDHPI) compounds were recently reported to be potent and selective negative allosteric modulators of GPR84.[18] The lead antagonist, GLPG1205, bound GPR84 with an inhibition constant of $K_i$ = 7.52 nM and reduced the disease activity score and human neutrophil infiltration ($IC_{50}$ = 11 nM) in a rodent model of inflammatory bowel disease. GLPG1205 also showed positive results in a Phase II clinical trial of patients with idiopathic pulmonary fibrosis.[19] Unfortunately, the chemical structure of GLPG1205 lacks a site for late stage $^{11}C$ incorporation for PET tracer synthesis. Thus, we hypothesize that closely related structural analogs of GLPG1205 will maintain selectivity for GPR84 and serve as high affinity PET tracers, allowing for assessment of this new potential imaging biomarker. Here, we report the radiosynthesis and characterization of two $^{11}C$-labeled radiotracers (**$^{11}$C-MGX-10S** and **$^{11}$C-MGX-11S**) based on the DDHPI chemical scaffold. After assessing both radiotracers in cells and healthy mice, we investigated the utility of the most promising candidate, **$^{11}$C-MGX-10S**, in a well-established mouse model of systemic innate immune activation.

## RESULTS AND DISCUSSION

### Optimized Synthesis Yielded Enantiopure Precursors and Cold Standards

In 2020, Labéguère et al. reported a library of GPR84 inhibitors.[18] From this library, we shortlisted two potential molecules for two main reasons: (1) structural amenability for incorporation of a $^{11}C$ isotope and (2) favorable CNS PET multiparameter optimization (CNS PET MPO) scores indicating their high potential for blood-brain barrier (BBB) permeability (Table S1). The CNS PET MPO score considers several physicochemical properties including molecular weight (MW), topological polar surface area (TPSA), and lipophilicity (Clog *P*) of the radioligands.[20,21] **$^{11}$C-MGX-10S** and **$^{11}$C-MGX-11S** have suitable MW (<400), TPSA (70−82), and Clog *D* (<2), yielding a cumulative score of 4.8/5.0 for **$^{11}$C-MGX-10S** and 4.1/5.0 for **MGX-11S**. These scores suggest that these radiotracers have a high likelihood of BBB penetration (Table S1). In pursuit of cold standards (for quality control using HPLC analysis) and precursors for $^{11}C$ labeling, we optimized a previously reported synthesis with several modifications (Scheme 1). Our synthetic route avoids late stage addition of the methyl group on the phenolic precursor, thereby circumventing the formation of side products *via* keto−enol tautomerization (see Supporting Information for reaction mechanism Figure SI 1). We obtained >95% pure products (assessed *via* NMR and HPLC; see Supporting Information Section 6 for NMR and Figure SI 2 for HPLC chromatographs) with overall yields of 17.27% (**MGX-10S**) and 32.55% (**MGX-11S**) in four steps. Precursors were generated by deprotection of the **MGX-3** methoxy group using boron tribromide at −78 °C to room temperature, followed by reprotection with an allyloxy group using ally bromide/potassium carbonate at room temperature, subsequent dioxane ring installation with dioxane alcohols at 0 °C, and finally deprotection of the allyloxy group with palladium (0) catalyst (see Supporting Information for the detailed procedure). The resulting precursors, **MGX-8S** and **MGX-9S**, were >95% pure (determined *via* NMR and HLPC; see Supporting Information Figure SI 2 for HPLC chromatographs) with overall yields of 19.83% (**MGX-8S**) and 22.28% (**MGX-9S**).

We also optimized the synthesis of (2*R*)-hydroxymethyl-2,3-dihydro-[1,4]dioxino[2,3-*b*]pyridine (**$R_2$**, see Scheme S1 in the Supporting Information)—an integral part of the **$^{11}$C-MGX-11S** radiotracer. The novel pathway involved a Mitsunobu reaction that transferred enantiomeric purity of the starting glycerol (**Compound 3-$R_2$**, Scheme S1) to **Compound 6-$R_2$** *via* intramolecular cyclization-induced complete inversion of the chiral center. We replaced the previously reported trityl-protecting group of the primary alcohol with *tert*-butyldiphenysilyl (TBDPS), which is more stable in acidic conditions and protects the scaffold from hydrolysis.[22]

### MGX-10S and MGX-11S Bind GPR84 at Nanomolar Concentration

To determine the affinity of the MGX-10S and MGX-11S compounds for human GPR84, we performed competition binding assays using [$^3$H]G9543.[23] Binding of [$^3$H]G9543 to membranes from Flp-In TREx 293 cells expressing a FLAG-human GPR84- G$\alpha_{i2}$ fusion protein was fully competed by the compounds **MGX-10S** and **MGX-11S** with $K_i$ in the nanomolar range; this was similar to that observed for the reference GLPG1205 ($K_i$ = 24.53 ± 14.26 nM, $K_i$ = 39.92 ± 12.83 nM and $K_i$ = 7.99 ± 3.40 nM, respectively; Figure 2A). Compounds **MGX-10S** and **MGX-11S** were also fully blocked in a concentration-dependent manner, and inhibition of forskolin-amplified cAMP levels was carried out by 2-HTP in the same cells ($IC_{50}$ = 104.70 ± 58.79 and 70.28 ± 36.28 nM, respectively; Figure 2B). We finally utilized this membrane system to demonstrate that **MGX-10S** and **MGX-11S** were each able, in a concentration-dependent manner, to fully block activation of human GPR84 promoted by 2-(hexylthiol)-pyrimidine-4,6 diol (2-HTP) in [$^{35}$S] GTP$\gamma$S binding assays with potency in the high nanomolar range ($IC_{50}$ = 250.40 ±


https://doi.org/10.1021/jacsau.3c00435
JACS Au 2023, 3, 3297−3310

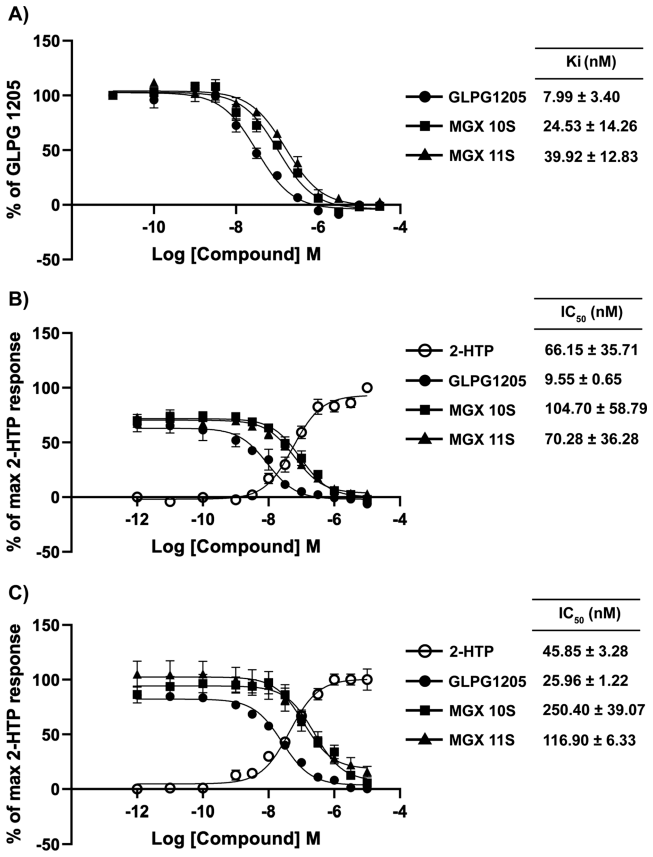


**Figure 2.** Binding and functional assays of cold standards. (A) Competitive binding assay with the known GPR84 inhibitor [$^3$H]G9543 using membranes from Flp-In TREx 293 cells expressing the human GPR84-G$\alpha_{i2}$ fusion protein ($n$ = 3). (B) cAMP assay using Flp-In TREx 293 cells expressing the human GPR84-G$\alpha_{i2}$ fusion protein ($n$ = 3). (C) GTP$\gamma$S assay: 3 mg of membranes from cells expressing the fusion human GPR84-Gi1/2 protein was used to pretreat compounds at increasing concentration and subsequently stimulated with a fixed concentration of the orthoseteric agonist 2-(hexylthiol)pyrimidine-4,6 diol (2-HTP). Data are expressed as mean ± standard error mean (SEM).

39.07 and 116.90 ± 6.33 nM, respectively; Figure 2C). These two functional assays confirmed that **MGX-10S** and **MGX-11S** are antagonists with high nanomolar $IC_{50}$. The high potency (low nanomolar binding affinity $K_i$) combined with moderate inhibitory effects (high nanomolar $IC_{50}$ values in the functional assays) predicts **$^{11}$C-MGX-10S** and **$^{11}$C-MGX-11S** as potential "Goldilocks" PET tracers.[24]

## Radiochemistry Yielded Pure Radiotracers with Sufficient Radiochemical Yield and High Molar Activity

To optimize radiolabeling, we screened various bases, temperatures, and sources of $^{11}$C (in the case of **$^{11}$C-MGX-10S** synthesis) (see Tables S2 and S3). The most optimal conditions for generating **$^{11}$C-MGX-10S** and **$^{11}$C-MGX-11S** involved the use of 1 M NaOH base (1.2 equiv) for 3 min at 65 and 110 °C, respectively (Scheme 2). Using these conditions, we achieved successful $^{11}$C labeling of the precursors with high radiochemical purity (>99%) and molar activity (17484.13 ± 6577.08 mCi/$\mu$mol for **$^{11}$C-MGX-10S** and 4116.03 ± 2335.71 mCi/$\mu$mol for **$^{11}$C-MGX-11S**) (Table 1) (see Figure SI 3 for Semipreparative HPLC chromatographs)

## $^{11}$C-MGX-10S and $^{11}$C-MGX-11S Specifically Bind Human GPR84 in Cells

With two new candidate GPR84 radiotracers in hand, we proceeded to assess their binding in cells with and without the expression of human GPR84. Cell binding studies revealed 14.5-fold higher binding of **$^{11}$C-MGX-10S** to hGPR84$^+$ HEK293 cells compared to parental HEK293 cells after 40 min of incubation ($n$ = 4, $P$ < 0.0001). A similar pattern was observed for radiotracer binding after 20 min incubation (Figure 3). Co-incubation of **$^{11}$C-MGX-10S** with the GPR84 antagonist GLPG1205 (35 $\mu$M) for 40 min significantly reduced radiotracer binding to hGPR84$^+$ HEK293 cells by 91.7%, demonstrating its high specificity ($n$ = 4, $P$ < 0.0001). In contrast, **$^{11}$C-MGX-11S** bound hGPR84$^+$ HEK293 cells with only a moderate 3.25-fold increase compared to the parental cells after 40 min of incubation ($P$ < 0.0001, $n$ = 4). The higher target to background binding of **$^{11}$C-MGX-10S** compared to **$^{11}$C-MGX-11S** could be due to the higher lipophilicity of **$^{11}$C-MGX-11S** (calculated *c*log $P$ = 0.963 vs *c*log $P$ = 0.313 for **$^{11}$C-MGX-10S**), which can lead to some potential nonspecific binding or it could be due to the higher affinity of **$^{11}$C-MGX-10S,** resulting in higher overall binding to cells expressing hGPR84 compared to **$^{11}$C-MGX-11S** (see Table S1). Co-incubation with GLPG1205 (35 $\mu$M) decreased **$^{11}$C-MGX-11S** binding by 91.5% ($P$ < 0.0001, $n$ = 4), indicating that while the overall binding is lower than **$^{11}$C-MGX-10S**, it is still specific for GPR84.

## $^{11}$C-MGX-10S and $^{11}$C-MGX-11S Cross the Blood−Brain Barrier of Healthy Mice

After evaluating our candidate GPR84 radiotracers *in vitro*, we compared their ability to cross the blood-brain barrier in healthy mice, finding the initial brain uptake (1 min postinjection) of **$^{11}$C-MGX-10S** to be higher than that of **$^{11}$C-MGX-11S** (Figure 4A). Co-registration of PET/CT images with a mouse brain atlas and subsequent quantification of the radioactive signal in the whole brain over time demonstrated rapid entry of **$^{11}$C-MGX-10S** into the brain with an average peak uptake of 5.90 ± 0.89%ID/g ($n$ = 4) within 22.5 s, decreasing to 1.89 ± 0.35%ID/g by the end of the 60 min scan, demonstrating favorable brain uptake with fast washout rate ($Brain_{1\ min/60\ min}$ > 3; illustrating that the uptake of **$^{11}$C-MGX-10S** in healthy mouse brain peaked within 1 min and that less than 1/3rd of the initial radiotracer activity remained at 60 min).[25] Whole body 3D maximum intensity projection (MIP) PET/CT images using **$^{11}$C-MGX-10S** illustrate a robust brain signal at 0−2 min with increasing renal/hepatic clearance, in addition to a low background signal in all other areas of the body, by the later time point (30−60 min) (Figure 4B,C). In contrast, **$^{11}$C-MGX-11S** displayed a lower and slightly slower peak brain uptake of 2.77 ± 0.71% ID/g within 52.5 s, which gradually decreased over the duration of the scan to 1.36 ± 0.14% ID/g with a slower brain washout rate ($Brain_{1\ min/60\ min}$ ∼ 2) than **$^{11}$C-MGX-10S**. We determined that **$^{11}$C-MGX-10S** has a more favorable kinetic profile for imaging GPR84 in the CNS than **$^{11}$C-MGX-11S** and that its ratio of peak uptake-to-levels at the end of the scan is comparable to, if not more favorable than, two other small molecule PET tracers used for clinical neuroimaging research studies, namely, $^{11}$C-UCBJ and $^{11}$C-Raclopride. $^{11}$C-UCBJ, a radiotracer that binds the synaptic vesicle glycoprotein 2A receptor and is used to image synaptic density, has a ratio of ∼3 in healthy mouse brain scans [the radiotracer reached


https://doi.org/10.1021/jacsau.3c00435
JACS Au 2023, 3, 3297−3310

Scheme 2. Radiosynthesis and HPLC Validation of $^{11}$C-MGX-10S and $^{11}$C-MGX-11S

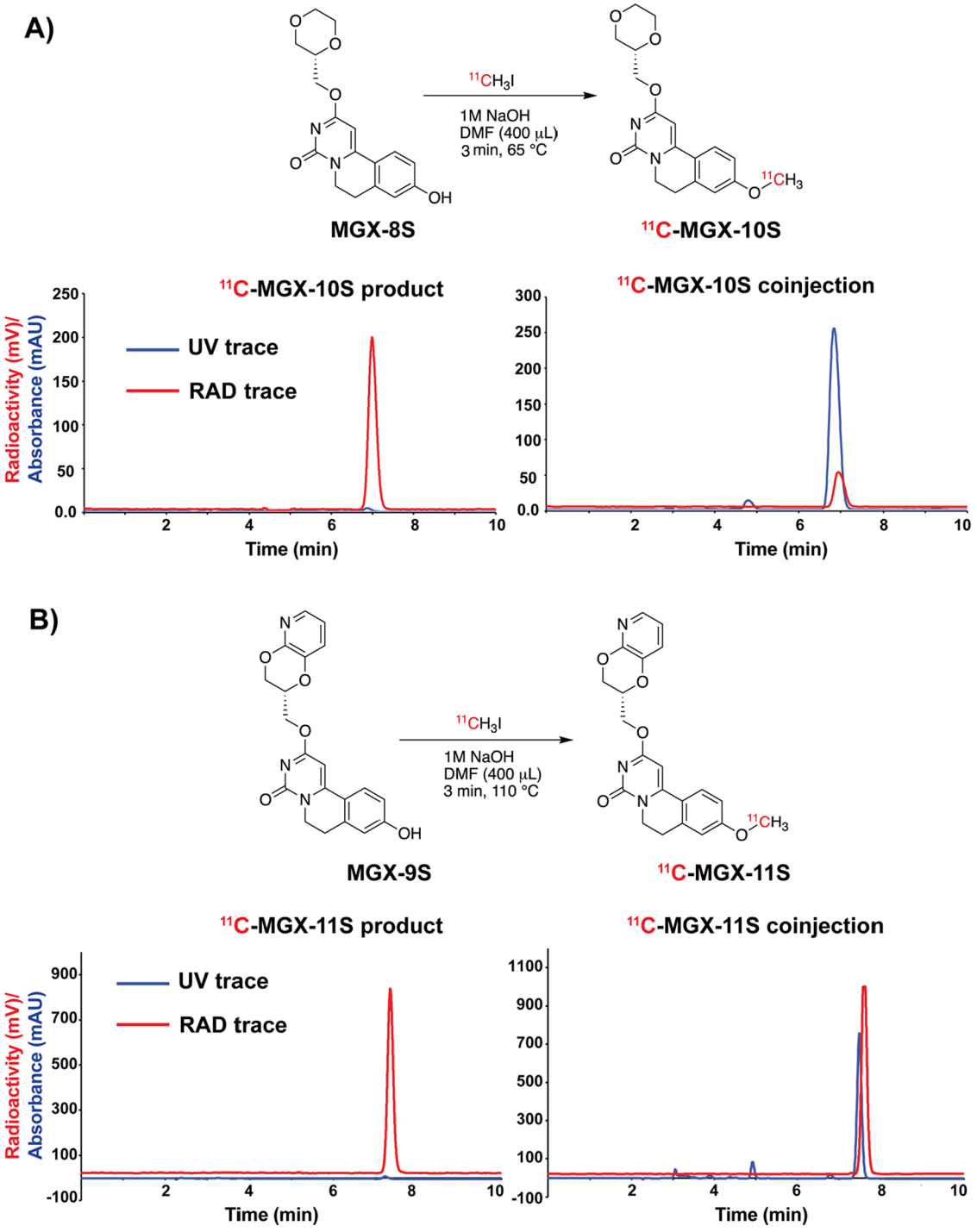


Table 1. Quality Control Summary of $^{11}$C Radiotracers

| radiotracers | end of synthesis radiochemical yield (without decay correction) (%) | radiochemical purity (%) | molar activity (mCi/μmol) |
|---|---|---|---|
| $^{11}$C-MGX-10S | 1.30 ± 0.40 ($n$ = 12) | >99 | 17484.13 ± 6577.08 ($n$ = 12) |
| $^{11}$C-MGX-11S | 1.16 ± 0.15 ($n$ = 3) | >99 | 4116.03 ± 2335.71 ($n$ = 3) |

maximum uptake at 15 min post-tracer injection and gradually cleared over a span of 90 min, with brain pharmacokinetics ($Brain_{15\ min/90\ min} \sim 3$)].[26] Another widely used CNS PET radiotracer, $^{11}$C-Raclopride, known to bind postsynaptic dopamine D2 receptors, achieved maximum uptake in 5 min in healthy rodents and gradually reached a plateau over 60 min with washout pharmacokinetics of $Brain_{5\ min/60\ min} \sim 2$.[27]

In summary, the favorable uptake and washout pharmacokinetics of $^{11}$C-MGX-10S radiotracer in healthy mice ($Brain_{1\ min/60\ min} > 3$) warranted further investigation of this radiotracer in a murine model of innate immune activation. As



https://doi.org/10.1021/jacsau.3c00435
JACS Au 2023, 3, 3297−3310

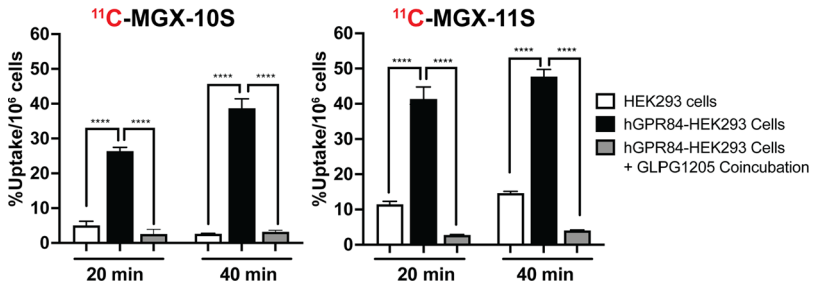


**Figure 3.** *In vitro* radiotracer binding specificity. Binding of **$^{11}$C-MGX-10S** and **$^{11}$C-MGX-11S** was assessed following incubation for 20 and 40 min with parental control cells or human-GPR84-expressing HEK293 cells in the presence or absence of GLPG1205 ($P < 0.0001$, $n = 4$ in each case). The radiotracer binding increased by 14.5-fold (**$^{11}$C-MGX-10S**) and 3.25-fold (**$^{11}$C-MGX-11S**) after 40 min of incubation. GLPG1205 (35 $\mu$M)—the most potent antagonist—blocked hGPR84 and reduced radiotracer binding more than 90%, establishing specific binding.

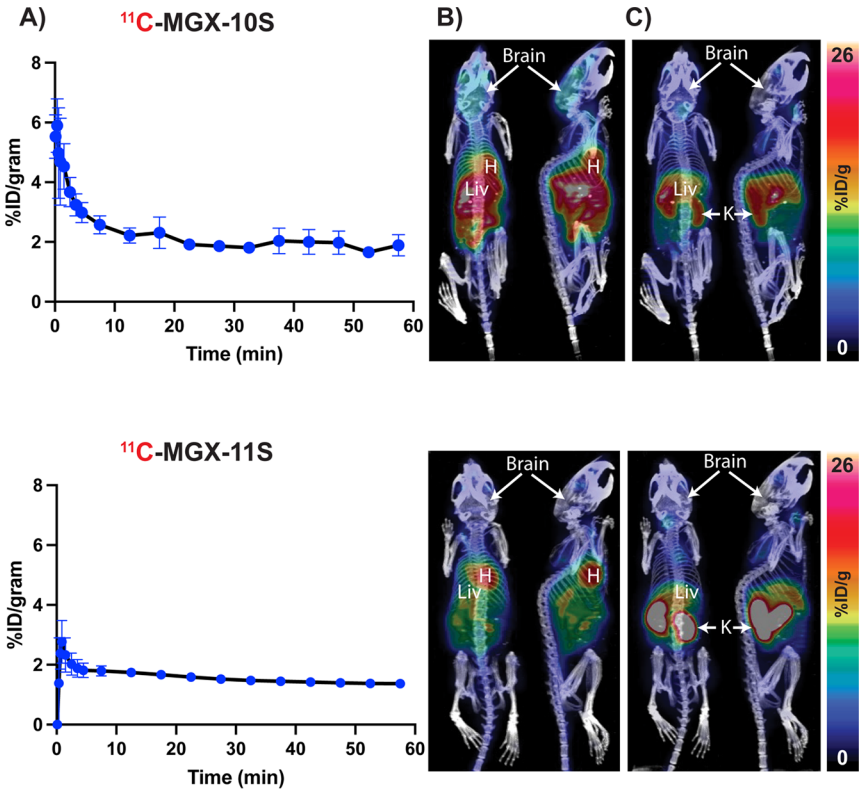


**Figure 4.** Blood–brain barrier permeability of $^{11}$C-MGX-10S and $^{11}$C-MGX-11S radiotracers. (A) Time-activity curves depicting *in vivo* uptake of **$^{11}$C-MGX-10S** (top) and **$^{11}$C-MGX-11S** (bottom) in whole mouse brain ($n = 4$) over the course of 60 min dynamic PET/CT imaging. Representative 3D maximum intensity projection PET/CT images illustrating the distribution of **$^{11}$C-MGX-10S** (top) and **$^{11}$C-MGX-11S** (bottom) in healthy mice summed over (B) 0–2 min and (C) 30–60 min. Br = brain, H = heart, K = kidney, and Liv = liver.

part of these studies, we assessed *in vivo* metabolic stability, biodistribution (*via* gamma counting), and *in vivo* specificity of **$^{11}$C-MGX-10S** in the brain *via* PET/CT imaging with and without blocking.

## Radiometabolite Analysis Shows Predominantly Intact $^{11}$C-MGX-10S in Brain

To investigate the metabolic stability of **$^{11}$C-MGX-10S** *in vivo* in the presence of inflammation, we administered saline (group 1) and LPS [5 mg/kg, intraperitoneal (i.p.), group 2] to C57BL/6 mice 24 h before radiotracer injection. At 5 and 20 min post-tracer injection, we performed the analysis of the whole brain and liver using analytical HPLC to assess the presence of potential radiometabolites. In saline-treated mice, **$^{11}$C-MGX-10S** was largely intact in the brain and liver at 5 min postinjection, with one polar metabolite, M1 peak (HPLC elution time = 2.8 min) in the plasma at this time. The tracer underwent low to moderate metabolism in the healthy brain, liver, and plasma 20 min postinjection, as reflected in the M1/parental peaks ratios (see Figure SI 4). Our analyses of LPS-treated mice revealed 100 and 97% intact radiotracer (parent radiotracer HPLC elution time = 5 min) in the brain at 5 min ($n = 3$) and 20 min ($n = 3$) post-tracer injection, respectively (Figure 5A). HPLC data of LPS mice plasma at 5 min postinjection showed the major parental peak while samples analyzed at 20 min postinjection revealed one metabolite M1 in addition to the parental peak (seeFigure SI 5). The inflamed mouse liver metabolized the radiotracer to some extent as the percentage of the intact radiotracer dropped from 100% to 90% within 20 min posttracer injection (Figure 5B). The action of cytochrome P450 (CYP)-3A4 and CYP2C19 enzymes in the liver likely resulted in the minor (10%)


https://doi.org/10.1021/jacsau.3c00435
JACS Au 2023, 3, 3297–3310

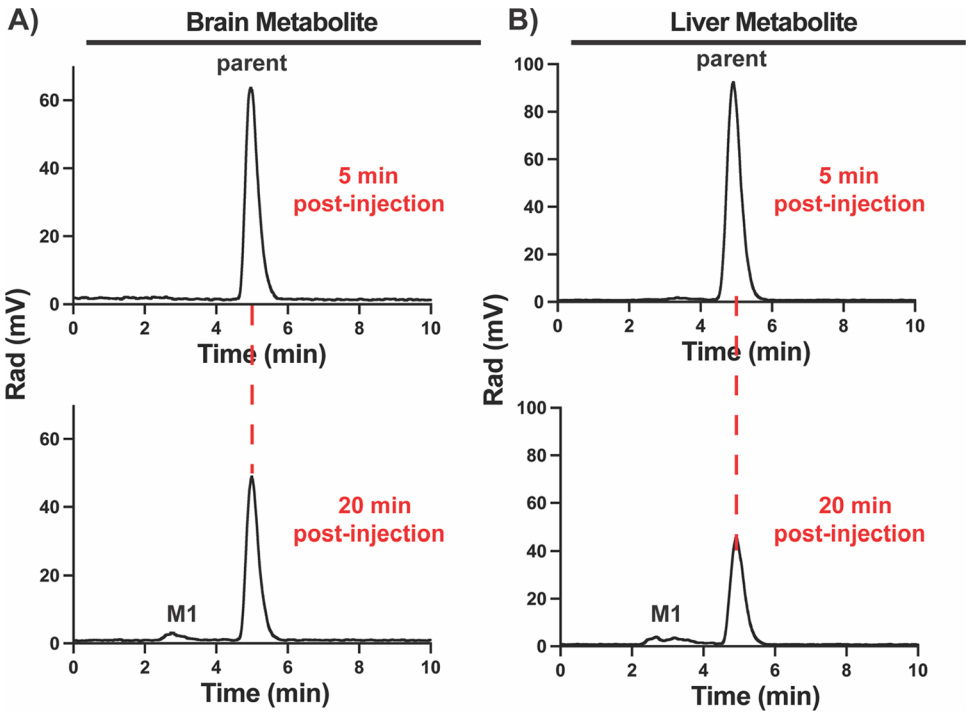


**Figure 5.** HPLC radiometabolite analysis to determine *in vivo* stability of $^{11}$C-MGX-10S. Radiotracer stability was assessed in mouse (A) brain and (B) liver at 5 min (top panel) and 20 min (bottom panel) post injection. 5 min postinjection HPLC analysis of the brain and liver samples showed a major radioactive parental peak (HPLC elution time = 5.0 min). 20 minutes postinjection HPLC analysis revealed a minor radiometabolite peak (M1 metabolite HPLC elution time = 2.8 min): 3% in brain and 10% in liver.

hydrophilic radiometabolite M1 (elution time = 2.8 min).[28] When compared between mouse and human liver microsomes and hepatocytes, unlabeled compound **MGX-10S** displayed 10-fold and 22-fold higher stability, respectively.[18] Based on these data, we predict that the intact $^{11}$C-MGX-10S radiotracer will persist longer in the human brain relative to the mouse brain.

## PET/CT Images Display Elevated Binding of $^{11}$C-MGX-10S in the Brain of LPS-Treated Mice

Administration of LPS intraperitoneally to mice is known to trigger rapid systemic inflammation in multiple peripheral organs, in addition to neuroinflammation as soon as 3 h after injection which can last up to 10 months, as evidenced by elevated levels of proinflammatory cytotoxic tumor necrosis factor alpha (TNF$\alpha$) and increased Iba1-positive immunostaining.[14] This rodent model of systemic inflammation has been used extensively to evaluate the ability of new radiotracers to accurately detect and quantify innate immune activation. Most recently, Horti et al. reported a $^{11}$C−CPPC radiotracer targeting CSF1R (a candidate biomarker of innate immune cell-driven inflammation) to have 55% higher binding in the mouse brain when injected with LPS (10 mg/kg) compared to a control animal.[29] This radiotracer displayed significant nonspecific binding since the CSF1R knockout mouse still showed an extensive signal.[28,30] Another example is the $^{11}$C-GSK1482160 radiotracer, which binds purinergic receptor subtype 7 (P2 × 7)—expressed on activated microglia induced by LPS (5 mg/kg) at a 3.2-fold higher amount than binding in saline-treated mice brains.[31] Although this is a promising fold difference in binding, P2 × 7 is a suboptimal biomarker for innate immune activation since it is not solely expressed on myeloid cells.[32] In the current work, we characterized the pharmacokinetics of **$^{11}$C-MGX-10S** in female C57BL/6J mice with and without LPS (5 mg/kg) treatment. Whole-body 3D MIP PET/CT images revealed a marked accumulation of **$^{11}$C-MGX-10S** in the brain, large intestine, liver, and stomach of the LPS-treated mice (Figure 6A; for 3D videos, see Supporting Information). We next focused on the brain to assess the ability of **$^{11}$C-MGX-10S** to detect neuroinflammation associated with this murine model. Whole brain time-activity curves (TACs) demonstrated rapid BBB penetration of the radiotracer in LPS-treated mice within 2 min and a sustained higher uptake compared to saline-treated mice (1.40-fold higher accumulation at 20 min and 1.42-fold higher by the end of the scan, $P < 0.05$) (Figure 6B). The 30−60 min integration of the whole brain PET signals of saline- and LPS-treated mice resulted marked increase in radiotracer uptake (approximately 39.27%, $P < 0.01$) in the LPS brain. All areas of the LPS-treated mouse brain displayed a significantly higher signal (except for the cerebellum), suggesting upregulation of GPR84 expressing immune cells in these tissues (see Figure SI 6). Notably, **$^{11}$C-MGX-10S** PET images clearly enable delineation of different disease severities [i.e., LPS score 0.5 (mild disease) versus 1.5 (severe disease)] (Figure 6C, for whole-body PET/CT; see Figure SI 7A)[33] and show dose-dependent blocking (Figure 6D, for whole-body PET/CT; see Figure SI 7B).

## $^{11}$C-MGX-10S Specifically Binds GPR84 *In Vivo* in the Context of Inflammation

Blocking studies were performed using the GLPG1205—a GPR84 antagonist being evaluated in clinical trials. A range of doses (0.65, 0.75, and 0.90 mg/kg) of GLPG1205 were used to investigate whether the blocking was dose-dependent. For this study, we injected LPS (5 mg/kg, i.p.) into mice ($n = 6$) 24 h before radiotracer injection. GLPG1205 was injected intravenously 10 min prior to radiotracer injection ($n = 4$).


https://doi.org/10.1021/jacsau.3c00435
JACS Au 2023, 3, 3297−3310

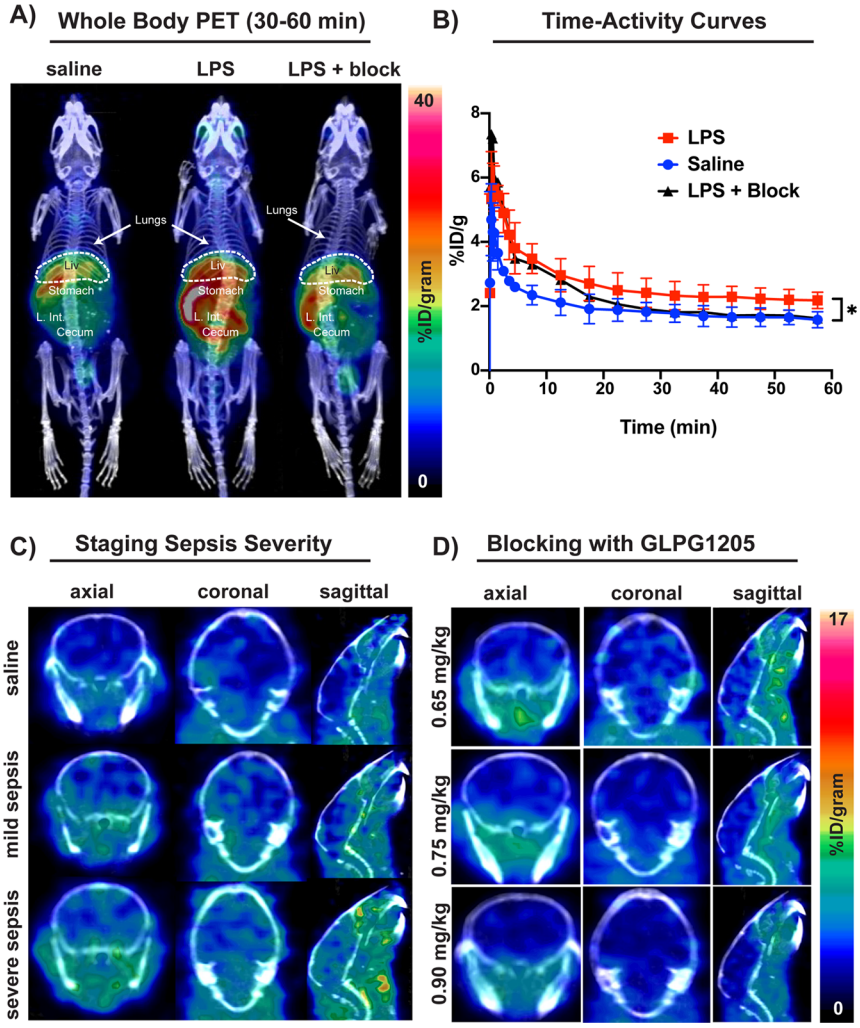


**Figure 6.** PET/CT images of activated innate immune responses in LPS-induced inflammation using $^{11}$C-MGX-10S. (A) Representative maximum intensity projection (MIP) whole-body images of saline ($n$ = 4), LPS ($n$ = 5) and LPS with GLPG1205 blocking ($n$ = 4) showed increased accumulation of the radiotracer in the LPS mouse and marked reduction in radiotracer uptake when GPR84 was blocked (summed 30−60 min). (B) Time-activity curves (TACs) of the whole brain from 60 min dynamic PET scan clearly shows rapid uptake of the radiotracer in the brain within 1 min of tracer injection followed by clearance. The radiotracer accumulated in the LPS brains 42.46% (at the end of the scan, $P < 0.05$) more than saline-treated brain. GLPG1205 (0.65 mg/kg) reduced this accumulation by 38.50% to the saline baseline at the end of the scan. (C) **$^{11}$C-MGX-10S** detected increased severity of innate immune responses and enabled neuroinflammation measurement (summed 30−60 min) as seen in the axial, coronal, and sagittal planes. (D) Dose-dependent blocking of GPR84 with GLPG1205 determined the radiotracer specificity in the brain. Liv = liver.

Preblocking with GLPG1205 markedly reduced whole-body radiotracer binding compared to mice administered LPS alone. The blocking agent (0.65 mg/kg) attenuated the PET signal in the LPS-treated mice brain by 38.50% at the end of the scan (Figure 6B). This reduction in the signal after GLPG1205 treatment is shown in the 30−60 min summed brain PET images, which illustrate a decrease in radiotracer binding almost to the level of the saline-treated mice brain. Dose-dependent GLPG1205 reductions in the brain PET signal were also observed (Figure 6D). This study clearly demonstrates the specific binding of **$^{11}$C-MGX-10S** to GPR84 in the mouse brain *in vivo*. Overall, these data suggest that **$^{11}$C-MGX-10S** has great promise for studying GPR84 expression in the brain in the context of inflammation.

## *Ex Vivo* Biodistribution Demonstrates Higher Radiotracer Accumulation in the LPS Brain

Whole-brain TACs suggest that **$^{11}$C-MGX-10S** binding in LPS mice begins to stabilize at ∼20 min post-tracer injection. Due to the short half-life of the $^{11}$C radiotracer ($T_{1/2}$ = 20 min) and its initial stable pharmacokinetics ($Brain_{20\ min/60\ min}$ ∼ 1.2), we assessed *ex vivo* biodistribution at 20 min postinjection of the radiotracer. TNF$\alpha$ production in the liver and blood of these mice ultimately triggers brain microglial activation, prompting proinflammatory protein synthesis.[14] These neuroinflammatory events portend high accumulation of **$^{11}$C-MGX-10S** in the blood, liver, and brain due to severe inflammation. Indeed, increased accumulation of **$^{11}$C-MGX-10S** was observed in several tissues from LPS-treated mice (including adipose tissue, blood, brain, heart, liver, lung, and spleen) compared to that in saline-treated mice. Specifically, we observed >1.8-fold increased radiotracer uptake in the brain (0.84 ± 0.21% ID/gram) and adipose tissue (1.16 ± 0.50% ID/g) of LPS-induced


https://doi.org/10.1021/jacsau.3c00435
JACS Au 2023, 3, 3297−3310

mice compared to those treated with saline (0.45 ± 0.06 and 0.63 ± 0.15% ID/g, respectively), consistent with known GPR84-mediated inflammatory processes in these tissues following LPS challenge.[34] The highest signal for both LPS- and saline-treated mice was observed in metabolic and excretory organs, including the liver (LPS: 7.08 ± 1.27% ID/gram, saline: 4.51 ± 0.15% ID/gram, $P < 0.05$) and kidneys (LPS: 8.73 ± 3.18% ID/gram, saline: 5.32 ± 3.01% ID/gram $P$ = not significant) indicative of a clearance pattern consistent with the kinetics of most small molecule radiotracers (Figure 7A).[35] The significant radiotracer accumulation in the liver likely represents LPS-induced inflammation in combination with radiotracer clearance.[36]

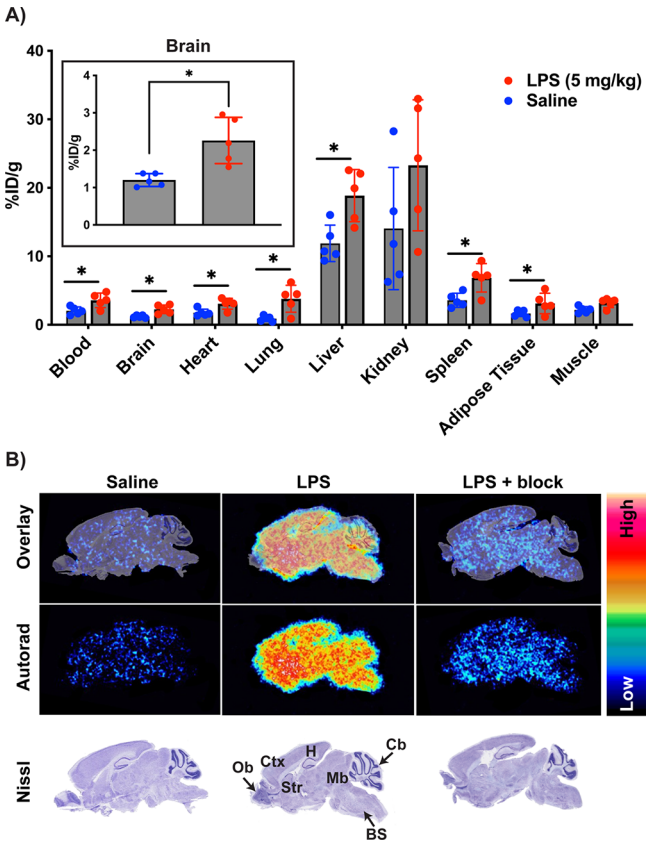


**Figure 7.** *Ex vivo* biodistribution and autoradiography. (A) **$^{11}$C-MGX-10S** radiotracer was administered in saline ($n$ = 5)- and LPS (5 mg/kg, $n$ = 5)-treated mice. At 20 min postinjection, animals were perfused with saline and tissues were collected, weighed, and gamma-counted. The LPS-induced systemic inflammation activated the innate immune response. The radiotracer accumulated in all organs, with the highest uptake in the liver and kidney. LPS mouse brains (0.84 ± 0.21% ID/gram) displayed ∼1.85-fold increase in radiotracer uptake compared to saline (0.45 ± 0.06% ID/g), suggesting overexpression of GPR84 on microglia. Statistical analysis was performed using "Unpaired $t$ test with Welch correction", *= $P < 0.05$. (B) *Ex vivo* autoradiography and histology validation of the **$^{11}$C-MGX-10S** radiotracer. This study highlights the specificity of our radiotracer in the brain. The LPS (5 mg/kg) brain retained marked radioactivity 20 min post injection compared to saline. The GLPG1205 antagonist blocked the radiotracer signal, suggesting GPR84 specific binding of **$^{11}$C-MGX-10S**. Cb = cerebellum, Ctx = cortex, Str = striatum, H = hippocampus, Mb = midbrain, Ob = olfactory bulb, and BS = brain stem.

Our results align with previous reports detailing elevated *gpr84* mRNA expression in adipose tissue, brain, and lung from mice treated with LPS (1 mg/kg). While this prior study did not use the same amount of LPS as we did in our study, nor did it investigate all the tissues we looked at, it serves to affirm, at least in part, what we observed. Bouchard and colleagues found a 4-fold increase in the brain *gpr84* at 24 h post-LPS compared to saline-injected mice. They applied in situ hybridization to show that *gpr84* mRNA expression was restricted to the leptomeninges and blood vessels 3 h after LPS treatment but was widespread throughout the brain at 24 h. This effect was absent following GPR84 antagonist treatments that partially block AKT and ERK phosphorylation and expression of proinflammatory cytokines (interleukin [IL]-6, IL-12b, and tumor necrosis factor [TNF]-$\alpha$), suggesting that pro-inflammatory cytokines likely regulate the endotoxin-induced GPR84 expression in the cerebral cortex of mice.[12,34]

## *Ex Vivo* Autoradiography Confirms $^{11}$C-MGX-10S Specificity

To obtain a high-resolution view of radiotracer distribution in the brain, we performed *ex vivo* autoradiography 20 min after **$^{11}$C-MGX-10S** injection. Brains from LPS-treated mice showed widespread radiotracer binding (matching previously published data on spatial *gpr84* expression in the brain of LPS-treated mice at this time point),[12] with slightly higher intensity in the striatum (Figure 7B). Preblocking with GLPG1205 (1 mg/kg) produced a dramatic reduction in the binding of **$^{11}$C-MGX-10S**, approximately to the level of the saline-treated mouse brain (Figure 7B). These results confirm the specificity of **$^{11}$C-MGX-10S** for GPR84 in the mouse brain.

## GPR84 PET Is More Sensitive Than TSPO PET

Next we compared **$^{11}$C-MGX-10S** with an existing clinical research radiotracer [$^{11}$C]N,N-Diethyl-2-[2-(4-methoxyphenyl)-5,7-dimethylpyrazolo[1,5-*a*]pyrimidin-3-yl]acetamide (**$^{11}$C-DPA-713**) that targets TSPO—a widely evaluated imaging biomarker of neuroinflammation.[37] In saline-treated mice, **$^{11}$C-DPA-713** concentrates in the kidneys, lungs, and spleen (all known to be TSPO-rich tissues). Unfortunately, the high TSPO-PET signal in many healthy tissues can make detection of early alterations in this target in the context of disease challenging and can obscure one's ability to visualize changes even under the most severe inflammatory conditions. For example, changes in the spleen signal in LPS-treated mice are difficult to delineate in TSPO-PET images due to the neighboring intense kidney signal (Figure 8A). To ascertain the sensitivity of **$^{11}$C-DPA-713** compared to our new GPR84 radiotracer, we directly compared their signal-to-background ratios using biodistribution data (expressed as a ratio of the signal in LPS to that in saline-treated mouse organs). While these data revealed similar brain uptake ratios for both radiotracers (**$^{11}$C-MGX-10S**: 1.86, **$^{11}$C-DPA-713**: 1.94, $P$ = not significant), **$^{11}$C-MGX-10S** afforded higher signal-to-background ratios than **$^{11}$C-DPA-713** in multiple inflamed peripheral organs including the liver (1.57 vs 0.86, $P < 0.005$), lungs (4.16 vs 1.48, $P < 0.05$), and spleen (1.89 vs 0.40, $P < 0.005$) (Figure 8B), signifying its ability to detect innate immune activation with higher sensitivity in these tissues. To investigate the reason for this observed higher sensitivity of our GPR84 radiotracer, we characterized the change in *gpr84* and *tspo* gene expression in the brains from saline- and LPS-treated (5 mg/kg) mice. Using qRT-PCR, we found that *gpr84* was upregulated to a greater extent than *tspo* (approximately 17-


https://doi.org/10.1021/jacsau.3c00435
JACS Au 2023, 3, 3297−3310

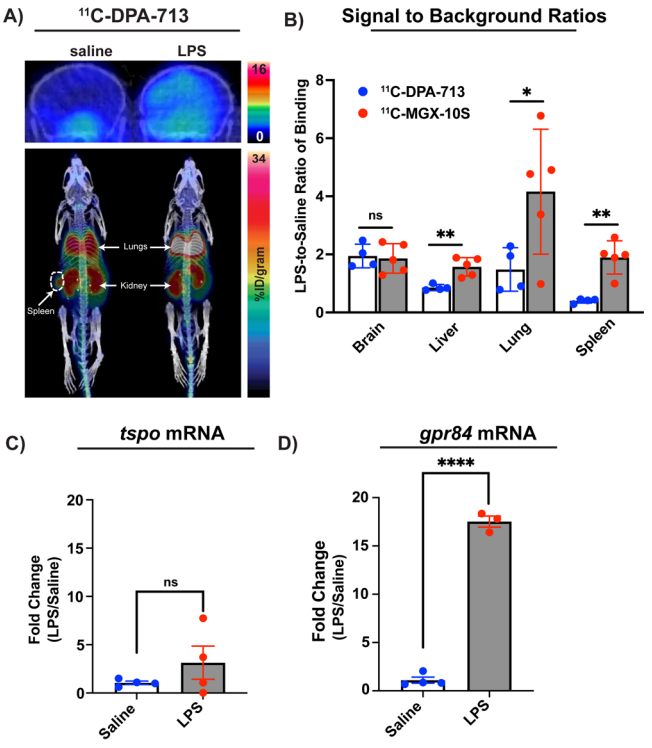


**Figure 8.** Comparison of GPR84 and TSPO PET radiotracers in a murine model of systemic innate immune activation. (A) *In vivo* PET imaging of TSPO *via* **$^{11}$C-DPA-713** enabled visualization of immune responses in the brain and peripheral organs in LPS-induced inflammation. Static PET images were acquired 50−60 min postinjection of **$^{11}$C-DPA-713.** (B) *Ex vivo* biodistribution of **$^{11}$C-MGX-10S** and **$^{11}$C-DPA-713** radiotracers revealed GPR84 and TSPO expressions respectively in brain, liver, lung, and spleen. Overall, **$^{11}$C-MGX-10S** performed better than **$^{11}$C-DPA-713** in liver ($P < 0.01$), lungs ($P < 0.05$), and spleen ($P < 0.01$)—known sites of activated immune cells and comparably in the brain and lung. (C) qPCR analysis of the *tspo* gene revealed no difference in its expression in LPS- and saline-treated mice ($n = 4$, $P$ = ns). (D) qPCR analysis of *gpr84* gene expression demonstrated significant upregulation in brains from LPS (5 mg/kg)-induced systemic inflammation compared to saline-treated mice ($n = 4$, $P < 0.0001$). Statistical analysis was performed using "Unpaired *t* test with Welch correction", *= $P < 0.05$, **= $P < 0.01$, ***= $P < 0.001$, ****= $P < 0.0001$.

fold change for *gpr84* versus 3-fold for *tspo*) in the brains of LPS-stimulated mice. (Figure 8C,D). These results support the high potential of GPR84 imaging to enable the sensitive detection of innate immune activation in neuroinflammatory diseases.

## CONCLUSIONS

Herein, we identified a proinflammatory orphan receptor known as GPR84 as a promising biomarker of detrimental innate immune activation. To image GPR84 and assess its utility as a PET biomarker, we synthesized two novel $^{11}$C radiotracers with high radiochemical yields and molar activity and evaluated their specificity *in vitro* and blood−brain barrier permeability *in vivo*. Based on the observed favorable brain uptake and pharmacokinetics of **$^{11}$C-MGX-10S**, we selected this radiotracer as our lead imaging agent to measure GPR84 expression associated with inflammation in a mouse model of systemic and neuro-inflammation. Our radiotracer displayed significantly higher binding in the brain and liver of mice treated with LPS (among other tissues), compared to mice treated with saline. Robust reduction in the PET signal was observed when mice were pretreated with GLPG1205 antagonist, affirming the specificity of **$^{11}$C-MGX-10S** for GPR84 in the context of inflammation. Importantly, our results using sensitive *ex vivo* techniques, including gamma counting and autoradiography, corroborated our *in vivo* PET imaging findings. Subsequently, we compared our new GPR84-targeting radiotracer with a widely studied TSPO-targeting radiotracer, **$^{11}$C-DPA-713**, and demonstrated the superior signal-to-background ratio of **$^{11}$C-MGX-10S** for identifying regions containing inflammation. Taken together, our work resulted in a new highly specific imaging tool for quantifying GPR84 *in vitro* and *in vivo*, and our data using this radiotracer underscore the high potential of GPR84-PET versus TSPO-PET for sensitive and specific detection of innate immune activation. Our studies have laid the foundation for future work involving other murine models of inflammatory diseases and human post-mortem tissues to further assess the promise of this radiotracer and GPR84 PET imaging for eventual clinical use.

## EXPERIMENTAL SECTION

### Animals

All animal procedures were approved by the Stanford Administrative Panel on Laboratory Animal Care (APLAC), accredited by the Association for the Assessment and Accreditation of Laboratory Animal Care (AAALAC International). All federal and state regulations governing the humane care and use of laboratory animals were upheld. For the subsequent experimental procedures, mice were anesthetized using isoflurane gas (2.0−3.0% for induction and 1.5−2.5% for maintenance). Female C57BL/6J wild-type mice were obtained from Jackson Laboratories. All animals were housed in a temperature-controlled environment under a 12-h light/dark schedule with ad libitum food and water access and were acclimatized for 1 week prior to experiments.

### Cell Culture

Human GPR84$^{+}$ HEK293 cells (Creative Biogene Biotechnology) were cultured in Dulbecco's modified Eagle's medium (DMEM; Life Technologies) containing 10% fetal bovine serum (Thermo Fisher Scientific, catalog 16000044) and puromycin (Thermo Fisher Scientific, catalog A1113803; 1 $\mu$g/mL). All cells were propagated at 37 °C in a humidified atmosphere containing 5% $CO_2$. Flp-IN TREx 293 cells expressing a GPR84-G$\alpha_{i2}$ fusion protein have been described previously.

### Quantitative PCR

Quantitative PCR (qPCR) was performed with SYBR Green Polymerase (Qiagen), RT-PCR Qiagen specified primers (TSPO, GPR84, and GAPDH), and cDNA. GAPDH was used as a housekeeping gene for all tissues. Reactions were completed on the Applied Biosystems QuantStudio 6 Real-Time PCR machine. Each sample was run with three technical replicates, and fold change for each gene was calculated by deriving $2^{ddCT}$. Transcripts with undetectable values were assigned a cycle threshold of 38 for analysis. Samples with high variation between technical replicates (SD > 0.70) were excluded from analysis.

### Precursors and Cold Standards Synthesis

Briefly, carbamate was produced by heating 2-(3-methoxyphenyl)-ethylamine and urea under acidic conditions for 2 days. The carbamate was reacted with diethylmalonate to afford hexahydropyrimidine-2,4,6-trione (**MGX-2**), which was transformed to dihydropyrimido[6,1-*a*]isoquinolin-4-one (**MGX-3**) by heating with phosphorus oxychloride ($POCl_3$) at 55 °C for 2 days. **MGX-3** was utilized as an intermediate for two parallel pathways—the HPLC standards (**MGX-10S** and **MGX-11S**) and the precursors (**MGX-8S**


https://doi.org/10.1021/jacsau.3c00435
JACS Au 2023, 3, 3297−3310

and **MGX-9S**). The HPLC standards were achieved by treating **MGX-3** with (***R***)-enantiomers of dioxane alcohol in the presence of potassium *tert*-butoxide at 0 °C for 30 min, followed by workup and column purification (see SI for detailed procedure).

## Radiosynthesis

We first optimized the $^{11}C$ labeling by screening different bases, base molar equivalences, and temperatures (see SI Tables S2 and S3). Next, the optimized conditions were applied to synthesize **$^{11}$C-MGX-10S** and **$^{11}$C-MGX-11S** using a GE TRACERLab FX M2 module. Trapped $^{11}CO_2$ was converted into $^{11}CH_3I$ in GE TRCAERLab FX MeI, and it was subsequently delivered to the FX M2 module. For **$^{11}$C-MGX-10S** synthesis, the precursor **MGX-7S** (0.63 mg, 1.907 $\mu$mol) and 1 M NaOH (2.28 $\mu$L, 1.2 equiv) base were reacted with $^{11}$C-methyl iodide in *N*,*N*-dimethylformamide (400 $\mu$L) for 3 min at 65 °C. For **$^{11}$C-MGX-11S** synthesis, **MGX-8S** (0.7 mg, 1.78 $\mu$mol) and 1 M NaOH (2.31 $\mu$L, 1.3 equiv) were treated with $^{11}$C-methyl iodide in *N*,*N*-dimethylformamide (400 $\mu$L) for 3 min at 110 °C. The reaction mixture was diluted with 1 mL of water and loaded on a semiprep HPLC for purification Phenomenex Gemini C18 column 5 $\mu$m, 110 Å, 250 × 10 mm) and purified using water +0.1% trifluoroacetic acid/acetonitrile +0.1% trifluoroacetic acid isocratic (70:30, 30 min). Each synthesis utilized identical formulation steps. The **$^{11}$C-MGX-10S** (elution time 12.5 min) or **$^{11}$C-MGX-11S** fraction (elution time 15.5 min) was collected into a round-bottom flask containing 20 mL water. This was then passed through a preconditioned Sep-Pak C18 Light cartridge (Waters). The loaded cartridge was washed with water (8 mL), and the radiotracer was eluted using ethanol (1 mL) and saline (4 mL). The total synthesis time was 60 min. The radiochemical purity and molar activity were determined *via* analytical HPLC (Phenomenex Gemini C18 column 5 $\mu$m, 110 Å, 250 × 4.6 mm) using water +0.1% trifluoroacetic acid/acetonitrile +0.1% trifluoroacetic acid isocratic (60:40, total run time = 12 min). For molar activity calculation, the area under the UV absorbance peak of the carrier product at 254 nm was compared to a standard curve of the cold standards (**MGX-10S** or **MGX-11S**).

## Binding Assays

FLAG-human GPR84-G$\alpha_{i2}$ fusion protein was generated as described previously.[23] Flp-In TREx 293 cells able to express in an inducible manner the FLAG-human GPR84- G$\alpha_{i2}$ construct were generated and maintained, and membranes were prepared as previously described.[23]

## Radioligand Displacement Assay

Assays were performed in the presence of 0.2 nM of [$^3$H]G9543 (corresponding to the radioligand $K_d$ concentration),[38] binding buffer [phosphate-buffered saline (PBS) with 0.5% fatty acid-free bovine serum albumin; pH 7.4], and the indicated concentrations of test compounds in a total assay volume of 500 $\mu$L in a 96-well plate. Binding was initiated by the addition of 5 $\mu$g of membranes, followed by incubation at 25 °C for 1 h, and subsequently terminated by the addition of ice-cold PBS and vacuum filtration through GF/C glassfiber filter-bottom 96-well microplates. Plates were washed three times with ice-cold PBS and then allowed to dry for 3h at room temperature. MicroScint-20 was added to dried filter plates, and radioactivity was quantified by liquid scintillation spectrometry.

**HTRF-Based cAMP Inhibition and [$^{35}$S]GTPγS Incorporation Assays** were performed as described in previous literature.[23]

## *In Vitro* Radiotracers Binding Assay

hGPR84$^+$ HEK293, and HEK 293 cells ($3 \times 10^5$) were plated into 12-well plates 16 to 24 h before **$^{11}$C-MGX-10S** or **$^{11}$C-MGX-11S** uptake analysis. On the day of the experiment, fresh, prewarmed DMEM (lacking FBS or antibiotic) containing approximately 0.925 MBq (or 25 $\mu$Curie) of **$^{11}$C-MGX-10S** (or **$^{11}$C-MGX-11S**) was added to each well (500 $\mu$L per well; 1.56 pmol). A GLPG1205 blocking solution of 35 $\mu$M final concentration was also prepared. The hGPR84+ HEK293 (± GLPG1205 block) and HEK cells were incubated with **$^{11}$C-MGX-10S** (or **$^{11}$C-MGX-11S**) at 37 °C and 5% $CO_2$ for 20 and 40 min ($n$ = 4). At the indicated time points, plates were placed on ice, washed three times with ice-cold PBS, and trypsinized (150 $\mu$L per well) for 2 min at 37 °C. The trypsin was neutralized by adding 600 $\mu$L of DMEM containing 10% FBS (original cell culture media) to each well. The cells from each well (500 $\mu$L) were transferred to gamma-counting tubes; a tube was also created containing a 500 $\mu$L standard of the radiotracer stock solution (1.85 MBq [or 50 $\mu$Curie]/mL). Gamma counting was performed to quantitate the percentage radiotracer uptake by the cells, and decay-corrected radioactivity was determined (Hidex automated gamma counter). Finally, cells in each gamma counting tube were counted by using the Countess cell counter (Life Technologies). Cell binding was expressed in terms of %uptake/million cells.

## Radiometabolite Analysis of $^{11}$C-MGX-10S

Mice were administered with LPS (5 mg/kg) or saline (100 $\mu$L) intraperitoneally (i.p.) approximately 24 h before radiotracer administration. **$^{11}$C-MGX-10S** was injected *via* the tail vein (650−1200 $\mu$Ci), while the mice were under anesthesia. Mice were perfused with PBS buffer (20 mL) under deep anesthesia. Whole blood was centrifuged at 1800 g for 4 min at room temperature to separate plasma (~200 $\mu$L), which was transferred to a 1.5 mL Eppendorf tube containing acetonitrile (300 $\mu$L) to precipitate plasma proteins. In the meantime, the whole brain and liver lobe were removed from each mouse and placed in two separate 50 mL Eppendorf tubes containing 500 $\mu$L acetonitrile, homogenized, and placed on ice. The well-homogenized samples were transferred to two 1.5 mL Eppendorfs, and the tubes containing plasma, brain, and liver were centrifuged at 9400 g for 4 min at room temperature; supernatants and pellets were subsequently transferred into distinct gamma counting tubes. All supernatants and pellets were counted using the gamma counter to measure extraction efficiency. Each supernatant (150−200 $\mu$L) was transferred directly into HPLC vials and injected for radio-metabolic analysis. A gradient mobile phase was used to accelerate the elution time of the **$^{11}$C-MGX-10S** radiotracer to 5 min. The gradient consisted of 50%A (0−6 min), 10%A (6.01−6.30 min), and 50%A (6:31−10 min), where Solvent A is water +0.1% trifluoroacetic acid/acetonitrile and Solvent B is 0.1% trifluoroacetic acid isocratic (60:40, total run time = 10 min). The column used was Phenomenex Gemini C18 column 5 $\mu$m, 110 Å, 250 × 4.6 mm).

## *Ex Vivo* Biodistribution

Mice were injected intraperitoneally with saline ($n$ = 5) or LPS (5 mg/kg) ($n$ = 5) approximately 24 h before radiotracer injection. Radiotracer was injected intravenously *via* the tail vein 24 h after LPS or saline administration, and mice were euthanized 20 min later. After perfusion, tissues of interest (adipocytes, blood, brain, heart, kidney, liver, lung, and spleen) were harvested, and weighed, and gamma counts were performed (Hidex automatic gamma counter, Hidex).

## PET/CT Imaging

We used a standard scoring system (murine sepsis score) to assess the symptoms after LPS challenge (see Table S4).[33] PET/CT imaging scans were carried out on GNEXT PET/CT (Sofie Biosciences) or Inveon D-PET (dedicated PET, Siemens) scanners. After a bolus intravenous injection of 100−500 $\mu$Ci (3.7−18.5 MBq) of **$^{11}$C-MGX-10S** into control and LPS mice (6.24−31.21 pmol), a 60 min dynamic PET scan was performed after administration of **$^{11}$C-MGX-10S**. The acquired list mode data were reconstructed into 19 frames (4 × 15, 4 × 60, and 11 × 300 s) using Iterative reconstruction method 3DOSEM-MAP (3D ordered-subset expectation maximization followed by fast maximum a posteriori (fastMAP) MAP (2; MAP subsets, 16; MAP iterations, 18). The TAC normalized to the injected dose was computed and expressed as %ID/g (% injected dose per gram). Image analysis was performed using commercial software (Scintica VivoQuant version 4.0), which is used to visualize radiotracer uptake and define the volumes of interest. MIP PET/CT images were created using another vendor software, Inveon Research Workplace software (Siemens).

## Autoradiography

Mice were administered LPS (5 mg/kg) or saline (100 $\mu$L) intraperitoneally. Approximately 24 h later, the **$^{11}$C-MGX-10S**



https://doi.org/10.1021/jacsau.3c00435
JACS Au 2023, 3, 3297−3310

radiotracer (800−1200 μCi) was administered intravenously; mice utilized in the blocking study were treated with GLPG1205 (1 mg/kg intravenous) 10 min prior to radiotracer administration. 20 minutes after radiotracer injection, each mouse was perfused with saline (20 mL) and brains were removed and snap-frozen in dry ice and then embedded in the optimal cutting temperature compound (Tissue-Tek, Sakura, U.S.). Next, brains were sectioned sagittally (60 μm) using a cryostat microtome HM500 (Microm, Germany). The sections were mounted on microscope slides (Fisherbrand Superfrost Plus microscope slides), air-dried for 10 min, and then exposed to phosphor imaging film (PerkinElmer, U.S.) for 12 h at 4 °C. The image plates were analyzed using a Typhoon 9410 variable mode imager (Amersham Biosciences, U.S.), and image data were visualized and processed by ImageJ (National Institute of Health). Anatomy of brain sections was confirmed by Nissl staining (cresyl violet acetate, Sigma-Aldrich).

### Statistical Analysis

Statistical analyses were performed by using GraphPad Prism (version 9). Cell binding assays and *ex vivo* biodistribution studies were analyzed by multiple unpaired Student's *t* test with Welch's correction. Data are expressed as the mean ± standard deviation (SD), unless otherwise indicated; a *P* value of 0.05 was considered significant.

## ■ ASSOCIATED CONTENT

### Supporting Information

The Supporting Information is available free of charge at https://pubs.acs.org/doi/10.1021/jacsau.3c00435.

Synthetic details for the precursors and HPLC standards, materials, and structural characterization data; analytical and semipreparative HPLC, NMR, and mass spectra of compounds (PDF)

3D maximum intensity PET/CT movies for representative mice from each group 30−60 min after injection of $^{11}$C-MGX-10S:

1) Saline-treated mouse (MP4)

2) LPS-treated mouse with mild sepsis (MP4)

3) LPS-treated mouse with severe sepsis (MP4)

4) LPS-treated mouse with severe sepsis, pre-blocked with GLPG1205 10 min prior to injecting $^{11}$C-MGX-10S (MP4)

## ■ AUTHOR INFORMATION


### Corresponding Author

**Michelle L. James** − *Department of Radiology and Department of Neurology and Neurological Sciences, Stanford University, Stanford, California 94305, United States*; Email: mljames@stanford.edu

### Authors

**Mausam Kalita** − *Department of Radiology, Stanford University, Stanford, California 94305, United States*; orcid.org/0000-0002-4847-2678

**Jun Hyung Park** − *Department of Radiology, Stanford University, Stanford, California 94305, United States*

**Renesmee Chenting Kuo** − *Department of Electrical Engineering, Stanford University, Stanford, California 94305, United States*

**Samira Hayee** − *Department of Radiology, Stanford University, Stanford, California 94305, United States*

**Sara Marsango** − *Centre for Translational Pharmacology, School of Molecular Biosciences, College of Medical, Veterinary and Life Sciences, University of Glasgow, Glasgow G12 8QQ, Scotland, U.K.*

**Valentina Straniero** − *Department of Pharmaceutical Sciences, University of Milan, 20133 Milano, Italy*; orcid.org/0000-0002-5089-0879

**Israt S. Alam** − *Department of Radiology, Stanford University, Stanford, California 94305, United States*

**Angelie Rivera-Rodriguez** − *Department of Radiology, Stanford University, Stanford, California 94305, United States*

**Mallesh Pandrala** − *Department of Radiology, Stanford University, Stanford, California 94305, United States*

**Mackenzie L. Carlson** − *Department of Neurology and Neurological Sciences, Stanford University, Stanford, California 94305, United States*

**Samantha T. Reyes** − *Department of Radiology, Stanford University, Stanford, California 94305, United States*

**Isaac M. Jackson** − *Department of Radiology, Stanford University, Stanford, California 94305, United States*; orcid.org/0000-0002-6928-7551

**Lorenzo Suigo** − *Department of Pharmaceutical Sciences, University of Milan, 20133 Milano, Italy*

**Audrey Luo** − *Department of Radiology, Stanford University, Stanford, California 94305, United States*

**Sydney C. Nagy** − *Department of Radiology, Stanford University, Stanford, California 94305, United States*

**Ermanno Valoti** − *Department of Pharmaceutical Sciences, University of Milan, 20133 Milano, Italy*

**Graeme Milligan** − *Centre for Translational Pharmacology, School of Molecular Biosciences, College of Medical, Veterinary and Life Sciences, University of Glasgow, Glasgow G12 8QQ, Scotland, U.K.*; orcid.org/0000-0002-6946-3519

**Frezghi Habte** − *Department of Radiology, Stanford University, Stanford, California 94305, United States*

**Bin Shen** − *Department of Radiology, Stanford University, Stanford, California 94305, United States*

Complete contact information is available at: https://pubs.acs.org/10.1021/jacsau.3c00435


### Author Contributions

CRediT: **Mausam Kalita** conceptualization, data curation, formal analysis, investigation, methodology, validation, visualization, writing-original draft, writing-review & editing; **Jun Hyung Park** data curation, formal analysis, methodology; **Renesmee Kuo** data curation, formal analysis, investigation; **Samira Hayee** formal analysis, investigation; **Sara Marsango** data curation, formal analysis; **Valentina Straniero** data curation, methodology; **Israt S Alam** data curation, visualization; **Angelie Rivera-Rodriguez** data curation, methodology; **Mallesh Pandrala** data curation, methodology; **Mackenzie L Carlson** data curation; **Samantha Reyes** data curation; **Isaac M Jackson** data curation; **Lorenzo Suigo** data curation, methodology; **Audrey Luo** data curation; **Sydney C Nagy** data curation; **Ermanno Valoti** resources, supervision; **Graeme Milligan** resources, supervision; **Frezghi Habte** data curation, supervision; **Bin Shen** methodology, supervision; **Michelle L. James** conceptualization, data curation, formal analysis, funding acquisition, investigation, project administration, resources, software, supervision, writing-review & editing.



https://doi.org/10.1021/jacsau.3c00435
*JACS Au* 2023, 3, 3297−3310

## Funding

M.L.J. and M.K. were supported by NIH/NINDS 1R21 AG07556501 for this work. G.M. and S.M. were supported by the Biotechnology and Biological Sciences Research Council UK (grant number BB/T000562/1).

## Notes

The authors declare no competing financial interest.

## ■ ACKNOWLEDGMENTS

The authors would like to thank Dr. Corinne Beinat for helpful discussion regarding radiometabolic assay. We also thank Cyclotron and Radiochemistry Facility (CRF) and Stanford Center for Innovation in In vivo Imaging (Sci3).

## ■ REFERENCES

(1) Hopperton, K. E.; Mohammad, D.; Trépanier, M. O.; Giuliano, V.; Bazinet, R. P. Markers of Microglia in Post-Mortem Brain Samples from Patients with Alzheimer's Disease: A Systematic Review. *Mol. Psychiatry* **2018**, *23*, 177−198.

(2) Absinta, M.; Maric, D.; Gharagozloo, M.; Garton, T.; Smith, M. D.; Jin, J.; Fitzgerald, K. C.; Song, A.; Liu, P.; Lin, J.-P.; Wu, T.; Johnson, K. R.; McGavern, D. B.; Schafer, D. P.; Calabresi, P. A.; Reich, D. S. A Lymphocyte-Microglia-Astrocyte Axis in Chronic Active Multiple Sclerosis. *Nature* **2021**, *597*, 709−714.

(3) International Multiple Sclerosis Genetics Consortium. Multiple Sclerosis Genomic Map Implicates Peripheral Immune Cells and Microglia in Susceptibility. *Science* **2019**, *365* (6460), No. eaav7188.

(4) Shi, K.; Tian, D.-C.; Li, Z.-G.; Ducruet, A. F.; Lawton, M. T.; Shi, F.-D. Global Brain Inflammation in Stroke. *Lancet Neurol.* **2019**, *18*, 1058−1066.

(5) Mrdjen, D.; Pavlovic, A.; Hartmann, F. J.; Schreiner, B.; Utz, S. G.; Leung, B. P.; Lelios, I.; Heppner, F. L.; Kipnis, J.; Merkler, D.; Greter, M.; Becher, B. High-Dimensional Single-Cell Mapping of Central Nervous System Immune Cells Reveals Distinct Myeloid Subsets in Health, Aging, and Disease. *Immunity* **2018**, *48*, 380−395.e6.

(6) Prater, K. E.; Green, K. J.; Mamde, S.; Sun, W.; Cochoit, A.; Smith, C. L.; Chiou, K. L.; Heath, L.; Rose, S. E.; Wiley, J.; Keene, C. D.; Kwon, R. Y.; Snyder-Mackler, N.; Blue, E. E.; Logsdon, B.; Young, J. E.; Shojaie, A.; Garden, G. A.; Jayadev, S. Human Microglia Show Unique Transcriptional Changes in Alzheimer's Disease. *Nat. Aging* **2023**, *3*, 894−907.

(7) Takamura, Y.; Kakuta, H. In Vivo Receptor Visualization and Evaluation of Receptor Occupancy with Positron Emission Tomography. *J. Med. Chem.* **2021**, *64*, 5226−5251.

(8) Nutma, E.; Ceyzériat, K.; Amor, S.; Tsartsalis, S.; Millet, P.; Owen, D. R.; Papadopoulos, V.; Tournier, B. B. Cellular Sources of TSPO Expression in Healthy and Diseased Brain. *Eur. J. Nucl. Med. Mol. Imaging* **2021**, *49*, 146−163.

(9) Vivash, L.; O'Brien, T. J. Imaging Microglial Activation with TSPO PET: Lighting Up Neurologic Diseases? *J. Nucl. Med.* **2016**, *57*, 165−168.

(10) Marsango, S.; Milligan, G. Regulation of the Pro-Inflammatory G Protein-Coupled Receptor GPR84. *Br. J. Pharmacol.* **2023**, DOI: 10.1111/bph.16098.

(11) Forsman, H.; Dahlgren, C.; Mårtensson, J.; Björkman, L.; Sundqvist, M. Function and Regulation of GPR84 in Human Neutrophils. *Br. J. Pharmacol.* **2023**, DOI: 10.1111/bph.16066.

(12) Bouchard, C.; Pagé, J.; Bédard, A.; Tremblay, P.; Vallières, L. G Protein-Coupled Receptor 84, a Microglia-Associated Protein Expressed in Neuroinflammatory Conditions. *Glia* **2007**, *55*, 790−800.

(13) Madeddu, S.; Woods, T. A.; Mukherjee, P.; Sturdevant, D.; Butchi, N. B.; Peterson, K. E. Identification of Glial Activation Markers by Comparison of Transcriptome Changes between Astrocytes and Microglia Following Innate Immune Stimulation. *PLoS One* **2015**, *10*, No. e0127336.

(14) Qin, L.; Wu, X.; Block, M. L.; Liu, Y.; Breese, G. R.; Hong, J.-S.; Knapp, D. J.; Crews, F. T. Systemic LPS Causes Chronic Neuroinflammation and Progressive Neurodegeneration. *Glia* **2007**, *55*, 453−462.

(15) Audoy-Rémus, J.; Bozoyan, L.; Dumas, A.; Filali, M.; Lecours, C.; Lacroix, S.; Rivest, S.; Tremblay, M.-E.; Vallières, L. GPR84 Deficiency Reduces Microgliosis, but Accelerates Dendritic Degeneration and Cognitive Decline in a Mouse Model of Alzheimer's Disease. *Brain Behav. Immun.* **2015**, *46*, 112−120.

(16) Nicol, L. S. C.; Dawes, J. M.; La Russa, F.; Didangelos, A.; Clark, A. K.; Gentry, C.; Grist, J.; Davies, J. B.; Malcangio, M.; McMahon, S. B. The Role of G-Protein Receptor 84 in Experimental Neuropathic Pain. *J. Neurosci.* **2015**, *35*, 8959−8969.

(17) Betlazar, C.; Harrison-Brown, M.; Middleton, R. J.; Banati, R.; Liu, G.-J. Cellular Sources and Regional Variations in the Expression of the Neuroinflammatory Marker Translocator Protein (TSPO) in the Normal Brain. *Int. J. Mol. Sci.* **2018**, *19* (9), 2707.

(18) Labéguère, F.; Dupont, S.; Alvey, L.; Soulas, F.; Newsome, G.; Tirera, A.; Quenehen, V.; Mai, T. T. T.; Deprez, P.; Blanqué, R.; Oste, L.; Le Tallec, S.; De Vos, S.; Hagers, A.; Vandevelde, A.; Nelles, L.; Vandervoort, N.; Conrath, K.; Christophe, T.; van der Aar, E.; Wakselman, E.; Merciris, D.; Cottereaux, C.; da Costa, C.; Saniere, L.; Clement-Lacroix, P.; Jenkins, L.; Milligan, G.; Fletcher, S.; Brys, R.; Gosmini, R. Discovery of 9-Cyclopropylethynyl-2-((S)-1-[1,4]-Dioxan-2-Ylmethoxy)-6,7-Dihydropyrimido[6,1-a]Isoquinolin-4-One (GLPG1205), a Unique GPR84 Negative Allosteric Modulator Undergoing Evaluation in a Phase II Clinical Trial. *J. Med. Chem.* **2020**, *63*, 13526−13545.

(19) Saniere, L.; Marsais, F.; Jagerschmidt, C.; Meurisse, S.; Cuzic, S.; Shoji, K.; Clement-Lacroix, P.; Van Osselaer, N.; De Vos, S. Characterization of GLPG1205 in Mouse Fibrosis Models: A Potent and Selective Antagonist of GPR84 for Treatment of Idiopathic Pulmonary Fibrosis. In *A19. Less Idiopathic: Structural and Functional Abnormalities in IPF*; American Thoracic Society: 2019; pp A1046−A1046.

(20) Wager, T. T.; Hou, X.; Verhoest, P. R.; Villalobos, A. Moving beyond Rules: The Development of a Central Nervous System Multiparameter Optimization (CNS MPO) Approach to Enable Alignment of Druglike Properties. *ACS Chem. Neurosci.* **2010**, *1*, 435−449.

(21) Wager, T. T.; Hou, X.; Verhoest, P. R.; Villalobos, A. Central Nervous System Multiparameter Optimization Desirability: Application in Drug Discovery. *ACS Chem. Neurosci.* **2016**, *7*, 767−775.

(22) Bolchi, C.; Pallavicini, M.; Fumagalli, L.; Moroni, B.; Rusconi, C.; Valoti, E. Univocal Syntheses of 2- and 3-Hydroxymethyl-2,3-Dihydro[1,4]Dioxino[2,3-b]Pyridine Enantiomers. *Tetrahedron: Asymmetry* **2005**, *16*, 3380−3384.

(23) Jenkins, L.; Marsango, S.; Mancini, S.; Mahmud, Z. A.; Morrison, A.; McElroy, S. P.; Bennett, K. A.; Barnes, M.; Tobin, A. B.; Tikhonova, I. G.; Milligan, G. Discovery and Characterization of Novel Antagonists of the Proinflammatory Orphan Receptor GPR84. *ACS Pharmacol. Transl. Sci.* **2021**, *4*, 1598−1613.

(24) Van de Bittner, G. C.; Ricq, E. L.; Hooker, J. M. A Philosophy for CNS Radiotracer Design. *Acc. Chem. Res.* **2014**, *47*, 3127−3134.

(25) Li, Y.; Zhou, K.; Zhang, X.; Zhao, H.; Wang, X.; Dong, R.; Wang, Y.; Chen, B.; Yan, X.-X.; Dai, J.; Sui, Y.; Zhang, J.; Cui, M. Fluorine-18-Labeled Diaryl-Azines as Improved $\beta$-Amyloid Imaging Tracers: From Bench to First-in-Human Studies. *J. Med. Chem.* **2023**, *66*, 4603−4616.

(26) Bertoglio, D.; Verhaeghe, J.; Miranda, A.; Kertesz, I.; Cybulska, K.; Korat, Š.; Wyffels, L.; Stroobants, S.; Mrzljak, L.; Dominguez, C.; Liu, L.; Skinbjerg, M.; Munoz-Sanjuan, I.; Staelens, S. Validation and Noninvasive Kinetic Modeling of [11C]UCB-J PET Imaging in Mice. *J. Cereb. Blood Flow Metab.* **2020**, *40*, 1351−1362.

(27) Alexoff, D. L.; Vaska, P.; Marsteller, D.; Gerasimov, T.; Li, J.; Logan, J.; Fowler, J. S.; Taintor, N. B.; Thanos, P. K.; Volkow, N. D. Reproducibility of 11C-Raclopride Binding in the Rat Brain Measured with the MicroPET R4: Effects of Scatter Correction and Tracer Specific Activity. *J. Nucl. Med.* **2003**, *44*, 815−822.

(28) Timmis, H.; Van Kaem, T.; Desrivot, J.; Dupont, S.; Meuleners, L.; Beetens, J.; Helmer, E.; Santermans, E.; Huettner, S. GLPG1205, a GPR84 Modulator: Safety, Pharmacokinetics, and Pharmacodynamics in Healthy Subjects. *Clin. Pharmacol. Drug Dev.* **2021**, *10*, 994−1006.
(29) Horti, A. G.; Naik, R.; Foss, C. A.; Minn, I.; Misheneva, V.; Du, Y.; Wang, Y.; Mathews, W. B.; Wu, Y.; Hall, A.; LaCourse, C.; Ahn, H.-H.; Nam, H.; Lesniak, W. G.; Valentine, H.; Pletnikova, O.; Troncoso, J. C.; Smith, M. D.; Calabresi, P. A.; Savonenko, A. V.; Dannals, R. F.; Pletnikov, M. V.; Pomper, M. G. PET Imaging of Microglia by Targeting Macrophage Colony-Stimulating Factor 1 Receptor (CSF1R). *Proc. Natl. Acad. Sci. U. S. A.* **2019**, *116*, 1686−1691.
(30) Altomonte, S.; Yan, X.; Morse, C. L.; Liow, J.-S.; Jenkins, M. D.; Montero Santamaria, J. A.; Zoghbi, S. S.; Innis, R. B.; Pike, V. W. Discovery of a High-Affinity Fluoromethyl Analog of [11C]5-Cyano-N-(4-(4-Methylpiperazin-1-Yl)-2-(Piperidin-1-Yl)Phenyl)Furan-2-Carboxamide ([11C]CPPC) and Their Comparison in Mouse and Monkey as Colony-Stimulating Factor 1 Receptor Positron Emission Tomography Radioligands. *ACS Pharmacol. Transl. Sci.* **2023**, *6*, 614−632.
(31) Territo, P. R.; Meyer, J. A.; Peters, J. S.; Riley, A. A.; McCarthy, B. P.; Gao, M.; Wang, M.; Green, M. A.; Zheng, Q.-H.; Hutchins, G. D. Characterization of 11C-GSK1482160 for Targeting the P2 × 7 Receptor as a Biomarker for Neuroinflammation. *J. Nucl. Med.* **2017**, *58*, 458−465.
(32) Tewari, M.; Seth, P. Emerging Role of P2 × 7 Receptors in CNS Health and Disease. *Ageing Res. Rev.* **2015**, *24*, 328−342.
(33) Shrum, B.; Anantha, R. V.; Xu, S. X.; Donnelly, M.; Haeryfar, S. M. M.; McCormick, J. K.; Mele, T. A Robust Scoring System to Evaluate Sepsis Severity in an Animal Model. *BMC Res. Notes* **2014**, *7*, 233.
(34) Recio, C.; Lucy, D.; Purvis, G. S. D.; Iveson, P.; Zeboudj, L.; Iqbal, A. J.; Lin, D.; O'Callaghan, C.; Davison, L.; Griesbach, E.; Russell, A. J.; Wynne, G. M.; Dib, L.; Monaco, C.; Greaves, D. R. Activation of the Immune-Metabolic Receptor GPR84 Enhances Inflammation and Phagocytosis in Macrophages. *Front. Immunol.* **2018**, *9*, 1419.
(35) Witney, T. H.; James, M. L.; Shen, B.; Chang, E.; Pohling, C.; Arksey, N.; Hoehne, A.; Shuhendler, A.; Park, J.-H.; Bodapati, D.; Weber, J.; Gowrishankar, G.; Rao, J.; Chin, F. T.; Gambhir, S. S. PET Imaging of Tumor Glycolysis Downstream of Hexokinase through Noninvasive Measurement of Pyruvate Kinase M2. *Sci. Transl. Med.* **2015**, *7*, 310ra169.
(36) Hamesch, K.; Borkham-Kamphorst, E.; Strnad, P.; Weiskirchen, R. Lipopolysaccharide-Induced Inflammatory Liver Injury in Mice. *Lab. Anim.* **2015**, *49*, 37−46.
(37) James, M. L.; Fulton, R. R.; Henderson, D. J.; Eberl, S.; Meikle, S. R.; Thomson, S.; Allan, R. D.; Dolle, F.; Fulham, M. J.; Kassiou, M. Synthesis and in Vivo Evaluation of a Novel Peripheral Benzodiazepine Receptor PET Radioligand. *Bioorg. Med. Chem.* **2005**, *13*, 6188−6194.
(38) Mahmud, Z. A.; Jenkins, L.; Ulven, T.; Labéguère, F.; Gosmini, R.; De Vos, S.; Hudson, B. D.; Tikhonova, I. G.; Milligan, G. Three Classes of Ligands Each Bind to Distinct Sites on the Orphan G Protein-Coupled Receptor GPR84. *Sci. Rep.* **2017**, *7*, 17953.


https://doi.org/10.1021/jacsau.3c00435
*JACS Au* 2023, 3, 3297−3310